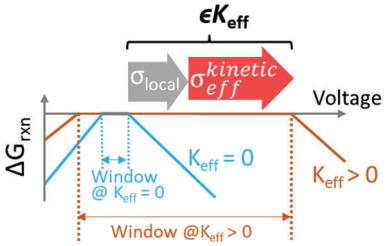


Dynamic voltage stability of solid-state battery interfaces widens the voltage stability window. It includes thermodynamic stability and a large portion of kinetic stability. The constrained ensemble computational approach is applied across most types of solid-state electrolytes to systematically evaluate and compare their dynamic stability voltage windows in response to the mechanical constriction effect and predict coating materials.

ADVANCED ENERGY MATERIALS
www.advenergymat.de

# Interface Coating Design for Dynamic Voltage Stability of Solid-State Batteries

*Yichao Wang, Luhan Ye, William Fitzhugh, Xi Chen, and Xin Li**

**Intrinsic or interface thermodynamic voltage windows of solid electrolytes are often narrower than the operational voltage range needed by a full battery, thus various interface decomposition reactions can happen in a practical solid-state battery. Experimentally, it is found that a proper battery design utilizing the reactions can lead to a dynamic evolution from interface instability to stability, giving the so-called dynamic voltage stability for advanced battery performance. Here, first the state-of-the-art understanding is articulated about how the dynamic voltage stability should be interpreted in physical picture and treated in computation, emphasizing the potential importance of nonequilibrium reaction pathways. The constrained ensemble computational approach is further applied across most types of solid-state electrolytes to systematically evaluate and compare their dynamic stability voltage windows in response to the mechanical constriction effect. High-throughput calculations are used to search for coating materials for different interfaces between sulfide, halide, and oxide electrolytes and typical cathode materials with enhanced dynamic voltage stability. A comparison with experiment is given to highlight the value of these computational predictions.**

## 1. Introduction

Solid-state battery is one of the most promising next-generate energy storage technologies, due to the potential to apply lithium metal anode for high energy density and much-improved safety by preventing lithium dendrite penetration.[1–4] For battery applications, the Li-ion conductivity, voltage stability window, and mechanical properties are three key electrolyte parameters. Mechanical properties of solid electrolytes are of particular interest in solid-state batteries. Low modulus of sulfides enables better contact between particles in the electrolyte and cathode mixture by a simple cold-press calendaring procedure.[5–7] More importantly, these three parameters are often strongly coupled in a solid-state battery to greatly influence electrochemical behaviors.

In theory, the strictest definition of voltage stability window refers to the voltage range that the electrolyte can work without any electrochemical decompositions thermodynamically. Precise calculations of such intrinsic voltage windows of various types of solid electrolytes have been performed previously.[8–12] However, in practice those intrinsic voltage windows are often narrower than the operational voltage range needed by a full battery, thus various decomposition reactions can still happen. This is especially true for sulfide solid electrolytes, where the intrinsic voltage window is only ≈1.7–2.3 V. Even considering the delithiation capacity in sulfide electrolyte, the effect can only widen the electrolyte voltage window to 2.5–3 V.[13–14]

In stark contrast, sulfide electrolyte-based solid-state batteries can cycle well in experiment in a wide voltage range with Li metal anode and 4 V cathodes, up to high current densities ≈50 mA $cm^{-2}$, and in a wide operational pressure range from several hundred MPa down to a few MPa.[2,4,15–20] These experimental facts suggest that certain stabilization mechanism must play a critical role here to widen the practical operational voltage window of solid-state batteries beyond the intrinsic voltage stability predicted by the standard convex hull computational approach.

It was found that for all-solid-state batteries, although small decomposition could happen beyond the intrinsic voltage window, they often show self-limiting decomposition, meaning that the decomposition can stop quickly at an early stage, giving the wide operational voltage stability in practice. This is in drastic difference to the case when the solid electrolyte is immersed in a liquid electrolyte, where the solid electrolyte decomposes deeply.[5] This is because in the former case any volume expansion decomposition reaction has to overcome the mechanical constriction imposed at the solid–solid interface by the all-solid environment, which is a critical factor that is missing in the latter case with liquid being added.

The local effective mechanical constriction modulus, $K_{eff}$, on the order of the bulk modulus of electrolytes has been proposed to strongly correlate with operational electrochemical stability through interactions with such positive reaction strains,[4–5,15,21–23] where the reaction strain has been observed experimentally together with advanced battery performance. Solid–solid interface under mechanical constriction was shown to be able to penalize decomposition reaction nuclei with an energy

Y. Wang, L. Ye, W. Fitzhugh, X. Chen, X. Li
John A. Paulson School of Engineering and Applied Sciences
Harvard University
Cambridge, MA 02138, USA
E-mail: lixin@seas.harvard.edu

The ORCID identification number(s) for the author(s) of this article can be found under https://doi.org/10.1002/aenm.202302288

**DOI: 10.1002/aenm.202302288**

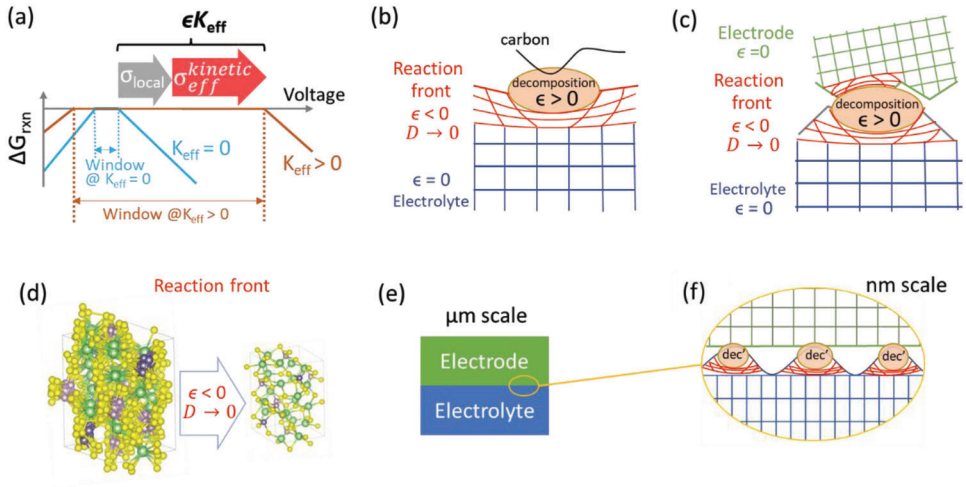


**Figure 1.** Illustration of dynamic voltage stability concept. a) Voltage stability window is opened by constriction with certain effective modulus ($K_{eff}$), where the effective stress $\epsilon K_{eff}$ is composed of an actual local stress ($\sigma_{local}$) and a kinetic contribution ($\sigma_{eff}^{kinetic}$) caused by kinetic stability; Decomposition nuclei of b) electrolyte or c) electrode–electrolyte interface will compress the reaction front and freeze the local ionic diffusivity ($D$). d) Due to compressive strain at the reaction front, the diffusivity of atoms drops dramatically, and the decomposition is kinetically stopped. e) Low porosity contacts of electrode and electrolyte at the micrometer scale. f) Solid–solid interface contact with many nanosized or sub-nanosized point contacts alternated by atomic scale gaps, giving inhomogeneous local chemical potential of lithium $\mu_{Li}(x)$ with strong spatial $x$ dependence and a development of plastic reaction strain that cannot be easily released.

scale on the order of $K_{eff}\epsilon V$, where $\epsilon$ is the local reaction strain and V is a reference volume. That is, the effect can lead to a dynamic evolution from interface instability to stability, giving the so-called dynamic voltage stability for advanced performance of solid-state batteries, where the operational voltage window of sulfide electrolytes is greatly widened when they are in contact with 4 V cathode and 0 V Li metal anode.[5,16,24]

In this work, we first articulate our state-of-the-art perspective on the thermodynamic and kinetic constitution of dynamic voltage stability. We broaden the meaning of $K_{eff}$ to include the kinetic stability, which allows the $K_{eff}\epsilon V$ energy penalty to effectively stabilize interface reactions when the local stress is smaller than the fracture limit. This is a critical development of our constrained ensemble description for interface reactions in solid-state batteries, since most solid electrolyte materials do not have a high fracture toughness,[25] but many of them can exhibit operational interface voltage stability way beyond the predicted limit of their thermodynamic voltage stability. We then further investigate the dynamic voltage stability for all the main types of Li solid electrolytes, including chalcogenides, oxides, halides, and borohydrides, as well as their interface stability with coating materials for classic oxide cathodes. Here we apply our constrained ensemble computations across these solid-state electrolytes (SSEs) to systematically evaluate and compare their dynamic stability voltage windows in response to the mechanical constriction effect. High-throughput calculations based on pseudo-binary approach are used to search for coating materials for different interfaces between electrolyte and cathode materials with enhanced dynamic voltage stability. This new strategy may design superior coatings to conventional ones that focus on electrochemical interface stability, as our design of dynamic in situ decomposition can fix any cracks induced by breathing cathode during battery cycling. Our analysis also emphasizes the importance of nonequilibrium reaction pathways, due to reaction kinetics controlled by various diffusion limiting processes at all-solid interfaces.

A comparison with experiment is given based on a readily available coating procedure for $LiNbO_3$ to demonstrate the unique prediction capability of our computational approach to design dynamic voltage stabilities by interface coatings. The detailed agreement between computation and experiment further highlights the potential value of the ≈150 new cathode coating materials predicted in this work. Our work thus will speed up the solid-state battery development by providing a promising list of candidate coating materials to the field with a potential to significantly stabilize the cathode interface reactions during the battery cycling.

### 1.1. Model and Perspective

Here, we first explain the physical meaning of the dynamic voltage stability using our state-of-the-art understanding and formula description, which forms the foundation for further high-throughput search and design of interface coating materials with enhanced such stability. The local effective modulus $K_{eff}$ and the effective stress $\sigma_{eff} = \epsilon K_{eff}$ describe the level of local mechanical constriction. It is important to note that the effective stress can often be larger than the actual local stress $\sigma_{local}$ (**Figure 1**a), because $\sigma_{eff} = \sigma_{local} + \sigma_{eff}^{kinetic}$, where the latter term $\sigma_{eff}^{kinetic}$ is an effective stress contributed by a kinetic diffusion-limiting process.

The plastic local strain field $\epsilon$ together with the actual local stress $\sigma_{local}$ from the initial local decomposition provide the common strain energy $E_{strain} \propto \sigma_{local}\epsilon V$ for thermodynamic metastability for any interface voltage reaction. More precisely, $E_{strain} = \int \sigma_{local}\, V d\epsilon$. However, the magnitude of the strain energy is limited by the plastic deformation and the fracture limit of electrolyte materials, beyond that there is no local mechanical

constriction. Simultaneously, at the reaction front, the same local inhomogeneous strain field $\epsilon$ can significantly decrease the ionic interdiffusion in the electrolyte by orders of magnitude to kinetically prevent further decomposition propagation, giving an ionic passivation effect from local reaction strain induced diffusion limiting process. Interface reactions will thus feel the significant effect from an additional energy stabilization term from the kinetic stability, $E_{\text{kinetic}}$, for wider interface voltage stability than what can be provided by thermodynamic metastability.

Since both energy terms of $E_{\text{strain}}$ and $E_{\text{kinetic}}$ share the same local reaction strain term $\epsilon$, we have $E_{\text{kinetic}} = \int \sigma_{\text{eff}}^{\text{kinetic}}\, V d\epsilon$, which defines the kinetic part of the effective stress $\sigma_{\text{eff}}^{\text{kinetic}}$. The total stabilization energy that includes both thermodynamic metastability and kinetic stability for interface reactions is thus $E_{\text{total}} = E_{\text{strain}} + E_{\text{kinetic}} = \int (\sigma_{\text{local}} + \sigma_{\text{eff}}^{\text{kinetic}})\, V d\epsilon$, which defines the total effective stress $\sigma_{\text{eff}} = \sigma_{\text{local}} + \sigma_{\text{eff}}^{\text{kinetic}}$. Since $\sigma_{\text{eff}} = \epsilon K_{\text{eff}}$, we thus also have $E_{\text{total}} = \epsilon K_{\text{eff}} V$ in the simplest form as the effective mechanical constriction energy.

More specifically, as illustrated in Figure 1b,c, the volume expansion decomposition with positive reaction strain ($\epsilon > 0$) compresses the surrounding electrolyte region, giving a local negative (compressive) strain ($\epsilon < 0$) at the reaction front of the undecomposed electrolyte. It was previously estimated that a 5% such local compressive strain will dramatically decrease the local ionic diffusivity $D$ by orders of magnitude,[22] giving a zero local diffusivity ($D \to 0$) at the reaction front in practice to shut down further interface reaction, as any solid-state decomposition will need sufficient ionic interdiffusion to happen kinetically (Figure 1b–d).

This kinetic stability mainly requires a positive reaction strain at a local reaction interface under mechanical constriction (i.e., low porosity at micrometer scale for good interface contact, as in Figure 1e), which in principle can be satisfied by most electrolytes upon a proper solid-state battery design. For sulfide or halide, for example, a cold press is often sufficient. However, even it is well constricted with low porosity at micrometer scale, at (sub)-nanometer scale the solid–solid interface between electrolyte and electrode materials can still be inhomogeneous spatially with a strong spatial $x$ dependence. This accordingly gives an inhomogeneous local lithium chemical potential $\mu_{\text{Li}}(x)$ due to the dry interface contact with many nanosized or sub-nanosized point contacts that are alternated by gaps at atomic scale (Figure 1f). In contrast, when a lithium-ion concentration is homogeneously surrounding a particle immersed in the liquid electrolyte, the solid electrolyte, and electrode form the classical liquid-solid surface contact rather than point contacts, instead giving a homogeneous local chemical potential of lithium.

Thus, in liquid electrolyte batteries, the reaction front can propagate deeply to consume the electrolyte,[5] as the reaction strain field is flat with small curvature that can be more easily released to the liquid environment, giving little effective stress to self-limit the decomposition. In contrast, in solid-state batteries, reaction strain was found to build up plastically without sufficient release. This is due to the inhomogeneous $\mu_{\text{Li}}(x)$, giving large local curvatures of the strain field (Figure 1f), where the local positive and negative strain fields are coupled and locked at the reaction front to give the self-limiting decomposition by the effective stress $\sigma_{\text{eff}}$.

The effective stress $\sigma_{\text{eff}} = \epsilon K_{\text{eff}}$ thus could be larger than both the actual local stress $\sigma_{\text{local}}$ and the fracture limit $\sigma_{\text{frac}}$ of the electrolyte materials without forming any actual fractures, as long as $\sigma_{\text{eff}} > \sigma_{\text{frac}} > \sigma_{\text{local}}$ is satisfied. In practice, it will also need the initial local decomposition to be suppressed quickly so that $\sigma_{\text{local}}$ is maintained at a low level, which is a property of interface reaction that can be designed. In addition, it also needs the electrolyte material to exhibit sufficient plastic deformation capability.

Therefore, in solid-state batteries there could be an important dynamic evolution of electrochemical process, where the local compressive strain at the reaction front induced by the tensile strain from initial decomposition will kinetically shut down the ionic diffusion locally by encapsulating the local decomposition by the ionically passivated reaction front layer, preventing further decomposition and crack formation. To design such interface reactions, technically, for any electrolyte material or its interface with electrodes, there is a critical effective modulus, $K_{\text{crit}}$[26] or $K^*$,[15] beyond that the local reaction can be fully suppressed. This critical modulus can be calculated by making $K_{\text{eff}}\epsilon V$ equal the decomposition hull energy $E_{\text{hull}}$, thus a smaller $K^*$ or $K_{\text{crit}}$ is preferred, as it suggests that the decomposition is easier to be suppressed by $K_{\text{eff}}$.

Importantly, we also point out here that since for a given decomposition hull energy $E_{\text{hull}}$, a larger local reaction strain $\epsilon$ will give smaller $K^*$ from $E_{\text{hull}} = K^* \epsilon V$, and simultaneously, larger $\epsilon$ also indicates stronger ionic passivation at the reaction front, looking for interfaces with smaller critical modulus $K^*$ thus also forms one important aspect to design the kinetic stability induced by the ionic passivation effect.

The above description forms our state-of-the-art understanding of the so-called dynamic voltage stability or simply dynamic stability that was proposed previously in an experimental work,[4] where advanced battery performance was demonstrated by utilizing the effect. This interpretation of dynamic voltage stability also goes beyond our previous works[5,15,26] by clearly stating that first, significant portion of the kinetic stability energy $E_{\text{kinetic}}$ is already included in the term of $K_{\text{eff}}\epsilon V$; second, the inhomogeneous local lithium chemical potential $\mu_{\text{Li}}(x)$ at the solid-solid interface is critical to the formation of the plastic reaction strain; and third, the quantitative condition of $\sigma_{\text{eff}} > \sigma_{\text{frac}} > \sigma_{\text{local}}$ needs to be satisfied to avoid fractures with sufficiently small local reaction stress, which however shares the same local reaction strain to simultaneously prevent further decomposition by sufficient effective stress. This interpretation forms an indispensable foundation for our computational approach to design dynamic stability presented in the following sections regarding intrinsic voltage stability window and interface coating materials that is of importance to the performance of solid-state batteries.

## 2. Results and Discussion

### 2.1. Electrolyte Dynamic Voltage Stability Window in Response to Constrictions

The dynamic voltage stability window of solid electrolytes is calculated by the minimization method (see Experimental Section). We systematically calculated the voltage window and reaction strain in response to mechanical constriction for three mainstream types of electrolytes, including sulfides, halides,

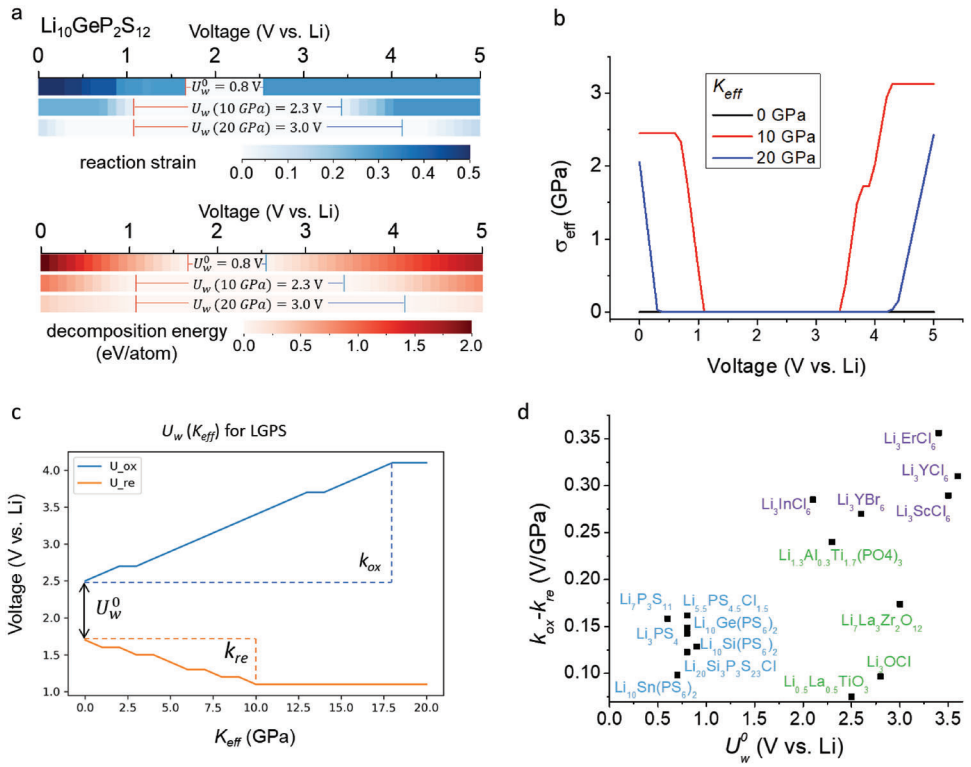


**Figure 2.** a) Electrolyte dynamic voltage stability window, reaction strain, and decomposition energy in response to constrictions by direct minimization method using LGPS as an example. The overall voltage stability window opens, and the reaction strain and decomposition energy decrease with increasing $K_{eff}$. b) The <4 GPa effective pressure $\sigma_{eff}$ induced by 0 to 5 V electrochemical decomposition under 0 to 20 GPa effective modulus $K_{eff}$ for LGPS. c) The metrics derived from the voltage window opening phenomenon: $k_{ox}$ and $k_{re}$ are the slopes by which the upper and lower stability limits of $U_{ox}$ and $U_{re}$ increase and decrease with increasing $K_{eff}$. d) The electrolyte distribution on the map of the window opening slope difference $k_{ox} - k_{re}$ ($k_{ox} > 0$ and $k_{re} < 0$) versus intrinsic voltage stability window.

and oxides (Figure S1, Supporting Information, for raw data). **Figures 2**a–c use $Li_{10}GeP_2S_{12}$ (LGPS) as an example to illustrate the phenomenon. Figure 2a shows the voltage stability window and the reaction strain at different voltages from 0 to 5 V and at different $K_{eff}$ of 0, 10, and 20 GPa. With increasing $K_{eff}$, the voltage window can be opened, as long as the reaction strain is positive at the voltage beyond the voltage window. Table S2 (Supporting information) shows more detail of decomposition energy, reaction strain, and decomposition product at 4 V at different $K_{eff}$.

Outside the stability window at a given voltage, the decomposition energy decreases with increasing $K_{eff}$. With increasing $K_{eff}$ the reaction strain also decreases and approaches zero eventually, giving the limit of voltage window opened by this process. However, since the driving force for decomposition also decreases with increasing $K_{eff}$, it makes nonequilibrium decomposition processes with larger reaction strains become more competitive and thus more likely to happen. Those nonequilibrium reactions thus may dominate the decomposition evolution pathway, which is an effect that could give an even wider operational voltage window in a properly designed practical battery than what can be predicted by the minimization method here.

Figure 2b shows the effective stress induced by electrochemical decomposition under different effective modulus $K_{eff}$ calculated by multiplying the modulus with the reaction strain in the minimization method. We emphasize that the effective modulus and effective stress, although with the unit of GPa, are different from the actual local stress. The effective stress is <3 GPa at 0–20 GPa $K_{eff}$ due to the <30% reaction strain at low $K_{eff}$ and the fact that with increasing $K_{eff}$ the reaction strain decreases. Since $\sigma_{eff} = \sigma_{local} + \sigma_{eff}^{kinetic}$ and the compliant yet brittle nature of sulfide,[25] it can be estimated that the magnitude of $\sigma_{local}$ is comparable to $\sigma_{eff}^{kinetic}$, and thus thermodynamic metastability and kinetic stability contribute comparably to the dynamic voltage stability of intrinsic voltage window.

Figure 2c analyzes the change of the oxidation limit $U_{ox}$ and reduction limit $U_{re}$ of LGPS with changing $K_{eff}$. $U_w^0$ is the intrinsic voltage window at zero constriction. $U_{ox}$ stops increasing at $K_{eff}$ = 18 GPa, while $U_{re}$ stops increasing at $K_{eff}$ = 10 GPa. We define $k_{ox}$ and $k_{re}$ as the two average slopes of $U_{ox}$ ($K_{eff}$) and $U_{re}$ ($K_{eff}$), where $k_{ox} > 0$ and $k_{re} < 0$. The slope difference $k_{ox} - k_{re}$ reflects the net voltage window opening rate with respect to the application of mechanical constriction $K_{eff}$, which can be considered as a metric to measure the susceptibility of the voltage window opening effect for different materials in response to mechanical constriction.

As shown in Figure 2d, sulfides and oxides show similar level of $k_{ox} - k_{re}$, while halides show higher $k_{ox} - k_{re}$ due to the high absolute value of both $k_{ox}$ and $k_{re}$ (Table S1 and Figure S1, Supporting Information). This suggests that halide electrolyte can show stronger voltage window openning effect in response to

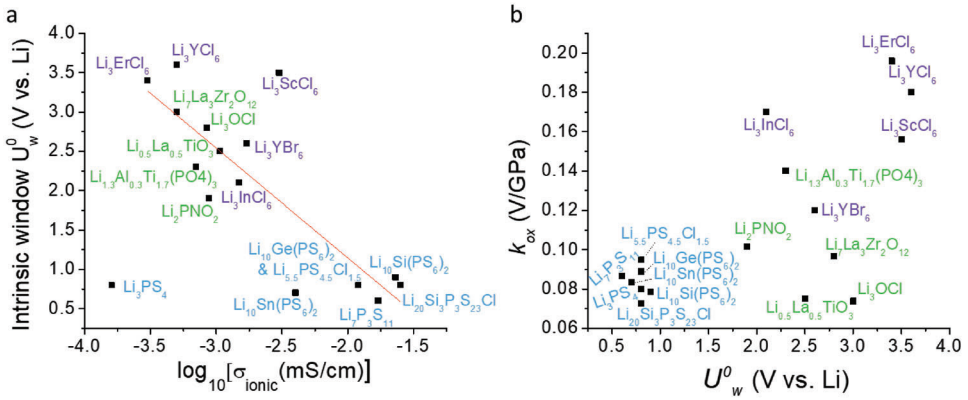


**Figure 3.** a) The negative correlation between the intrinsic window and the logarithmic Li ion conductivity.[6,7,27–39] b) The electrolyte distribution on the map of the opening slope at oxidative voltage limit $k_{ox}$ versus intrinsic voltage stability window.

mechanical constriction compared with sulfide electrolyte. For oxide electrolyte, at the reduction side $k_{re}$ is almost zero, which suggests that oxide solid electrolyte may benefit less from the dynamic voltage stability against lithium dendrite penetration that was found in sulfide and halide. However, oxides show $k_{ox}$ values between sulfides and halides, suggesting the constriction effect may still play a role at the cathode side for oxide electrolyte if the solid-solid interface between electrolyte and cathode particles can be well constricted, i.e., forming a good interface contact.

For $U_w^0$, the values for sulfides are the lowest, while oxides and halides with stronger chemical bonding due to higher electronegativity of $O^{2-}$, $Cl^-$, and $Br^-$ show much higher $U_w^0$. Therefore, in the ($k_{ox} - k_{re}$) versus $U_w^0$ plot (Figure 2d), sulfides, oxides, and halides occupy the bottom left region, middle-bottom right region, and top right region, respectively.

**Figure 3**a shows an interesting negative correlation between intrinsic voltage window $U_w^0$ and the logarithmic ionic conductivity. Sulfide occupies the bottom right corner, while oxides and halides occupy along the linear fitting line toward the top left region. A general picture for this relationship is that the fast lithium ion conduction in sulfide electrolyte is strongly contributed by certain soft phonon modes and their anharmonic couplings,[40] which meanwhile also imply relatively weak bonding that reduces the intrinsic stability of the electrolyte, thus giving the narrower intrinsic voltage window for sulfides.[41]

Since $k_{re}$ is zero only for oxide, for a fair comparison with halide and sulfide, we plot $k_{ox}$ v.s. $U_w^0$ in Figure 3b. The two correlations here (Figure 3a,b) suggest that electrolyte materials with high voltage opening susceptibility to mechanical constriction often tend to show low ionic conductivity together with hard phonon mode and chemical bonding. However, the fact that sulfide electrolytes can already show sufficient dynamic voltage stability suggests that when looking for new materials a $k_{ox}$ or $k_{re}$ value at the level of sulfide ≈0.1 V $GPa^{-1}$ is sufficient and higher such susceptibility value will likely come at an expense of reduced ionic conductivity.

**Figure 4** shows the voltage stability and reaction strain at different $K_{eff}$ of three types of solid electrolytes. Previously an inclusion or nucleation decay model was used to describe the decomposition inside a constricted LGPS,[22] which can be applied to the decomposition everywhere inside a theoretically dense pellet of polycrystalline SSE. According to the inclusion model, $K_{eff} \approx 0.5\ K_v$ where $K_v$ is the bulk modulus of the SSE, which gives $K_{eff}$ ≈15–20 GPa for sulfides, $Li_3ClO$ and $Li_3BrO$, and above 50 GPa for other oxides. Intermediate constriction values of $K_{eff}$ = 10 or 20 GPa are also considered for comparison. One obvious trend for all the electrolytes in Figure 4 is that at each voltage beyond the voltage window, the reaction strain becomes smaller with increasing $K_{eff}$, which is due to the larger energy penalty for larger-strain reactions in the reaction space at higher constriction level. This also reveals that here the smaller-strain reactions are the energetically more preferred.

### 2.1.1. Sulfides

The results of seven representative sulfides are shown by the blue bars. Most of their oxidative limits can be opened from ≈2.5 V to >3 V. LGPS and $Li_{5.5}PS_{4.5}Cl_{1.5}$ (LPSCl) can be opened to >4 V. The effect of mechanical constriction on glass sulfides, glass-ceramic sulfides, thio-LISICON, including $Li_3PS_4$, $Li_7P_3S_{11}$, LGPS, LSPS have been retrospectively reviewed,[23] suggesting that constriction induced voltage stability should have been a key concept in sulfides since the first glassy-ceramic sulfides.

Noted that other than LGPS and $Li_{5.5}PS_{4.5}Cl_{1.5}$, the oxidative limits do not or barely further increase with the increase of $K_{eff}$ from 10 to 20 GPa. This is due to the existence of decomposition with negative reaction strains (defined to be 0 in calculation, as discussed in Experimental Section) shown by the light-blue color above the oxidative limit, causing no voltage stability in response to constriction. In these cases, in addition to the limit of the minimization method discussed earlier, dynamic voltage stability can be further adjusted by using the strategies of coating or more generally the interface composition modification, as we will discuss in part B. Briefly, the requirement of $K_{eff}$ can be lowered for a given oxidative limit, as long as higher reaction strain can be obtained from other nonequilibrium processes or designed to such an interface through coating strategies, so that the decomposition can be more easily suppressed (i.e., reducing the critical effective modulus $K^*$).[15,26]

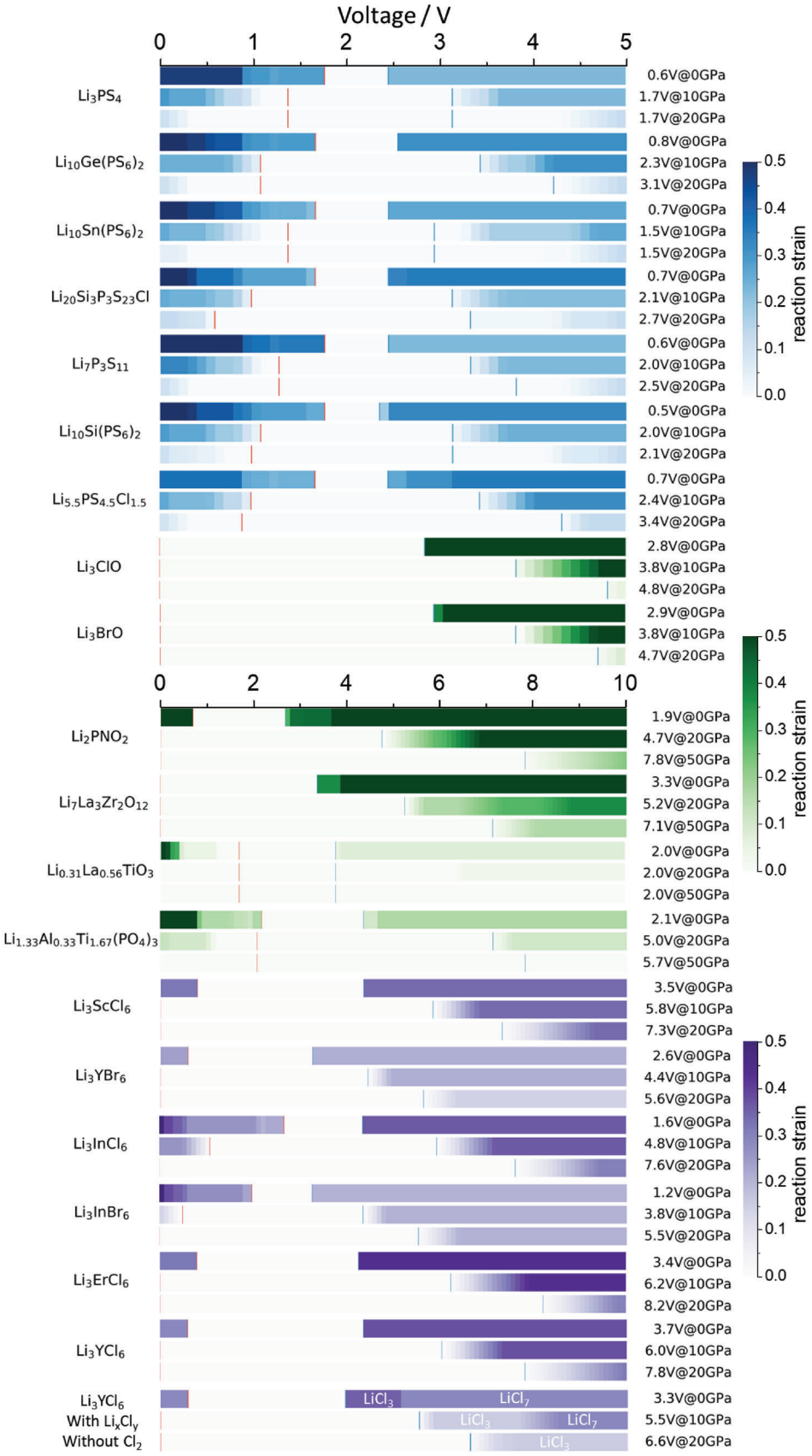

#### 2.1.2. Oxides

The result of six representative oxides is shown by the green bars in Figure 4, including anti-perovskite type $Li_3OCl$ and $Li_3OBr$, LIPON type $Li_2PNO_2$, garnet type $Li_7La_3Zr_2O_{12}$ (LLZO), perovskite type $Li_{0.5}La_{0.5}TiO_3$ (LLTO), and NASICON type $Li_{1.33}Al_{0.33}Ti_{1.67}(PO_4)_3$ (LATP). Oxidative limits can be raised close to 5 V or even >7 V, except for LLTO that decomposes to Li, $LiO_8$, $TiO_2$, $Li_2TiO_3$, $La_2Ti_4O_9$, and $La_2Ti_2O_7$ with negative reaction strain at 4.3 V at 10 GPa, limiting its oxidative limit at 4.3 V. Note that at 0 K from density functional theory (DFT) computations, oxygen molecule crystal (13.5 Å$^3$ atom$^{-1}$) appears in the decomposition products of LLZO (11.6 Å$^3$ atom$^{-1}$), LLTO (12 Å$^3$ atom$^{-1}$), and LATP (12.3 Å$^3$ atom$^{-1}$), but the atomic volume of the oxygen is not too far from the electrolytes, so the reaction strain in our calculation here is not provided by the possible gas phase at room temperature (RT). For high modulus oxides such as LIPON, LLZO, and LATP, to examine the effect of mechano-electrochemistry, it is important to get a dense electrolyte pellet with lowest possible porosity. Techniques such as pulsed laser deposition or coating deformable materials under cold press at interface are thus needed for these oxides.[42] In addition, whether these electrolytes can exhibit sufficient plastic deformation upon local decomposition is yet to be investigated, which may be another factor to limit the expansion of voltage window by $K_{\text{eff}}$.

Noted that $Li_3OCl$ and $Li_3OBr$ are with low enough modulus to be cold-pressed into a dense pellet and have a 4.8 V oxidative limit at $K_{eff} \approx 0.5\ K_v$. Together with high Li conductivity on the order of $10^{-3}$–$10^{-2}$ mS cm$^{-1}$ [39,43,44] they are also very promising high voltage electrolytes. In computation, the decomposition products are Li, LiCl, $LiClO_4$ beyond oxidative limit at $K_{eff}$ from 0 to 20 GPa. Experimentally, trace amount Ba doped $Li_3ClO$ has shown high RT Li conductivity of 25 mS cm$^{-1}$, and its oxidative limit is measured to be >8 V even at 130 °C.[43] The much wider 8 V stability than the 4.8 V stability in our computation could be due to the high kinetic barrier in forming the high valence $Cl^{7+}$ in the decomposition product of $LiClO_4$. Other potential decomposition products in Li-Cl-O system could be non-solid $Cl_xO_y$ that become energetically competitive at RT than the 0 K products, which result in larger reaction strain and thus a dynamic voltage window beyond 4.8 V. Therefore the 8 V stability of $Li_3ClO$ could be due to such extra kinetic stability at RT.

#### 2.1.3. Halides

Six halide electrolytes of $Li_3MX_6$ (M = Y, In, Er, Sc, X = Cl, Br) are considered. Their oxidative decomposition products are always Li, $MX_3$, and $X_2$ and the increase of reaction strain in a few tens of volts above the oxidative limit is due to the increasing portion of partial decomposition of $Li_3MX_6$ in the multi-phase equilibrium region of Li-M-X grand potential phase diagram. If there is any $Cl_2$ gas release in such a battery, the contribution from the volume of $Cl_2$ to reaction strain will disappear, causing negative reaction strain of ≈ −15%, thus probably no broadening of voltage window above 4.3 V. As the data in Materials Project are calculated at 0 K, $Cl_2$ is crystalized molecules cluster. Removing $Cl_2$ from decomposition products in computation will give infinite oxidation limit since other compounds in the Li-M-X systems cannot compose a balanced reaction equation due to the lack of Cl-rich phases. Note that Cl-rich $Na_xCl_y$ phases, i.e., $NaCl_3$ and $NaCl_7$ can form under GPa order of pressure,[45] Cl-rich $Li_xCl_y$ counterparts may also exist and can form under GPa level mechanical constriction. As there is no report on $Cl_2$ gas release experimentally, it is possible that halide electrolytes are either well constricted in batteries so that it is stable, or Cl-rich $Li_xCl_y$ phases are formed during decomposition. In the latter case, the predicted voltage window is shown at the bottom of Figure 4 with $Li_xCl_y$ phases labeled in the corresponding voltage range where the related decomposition happens. Although the voltage window shrinks a little when unconstrained, it can still open to 6.6 V at 20 GPa level of local mechanical constriction. Similar scenarios may happen for Li-M-Br electrolytes as $Br_2$ is in the liquid state at room temperature. These nonequilibrium reaction pathways are more likely to happen under diffusion limiting condition from mechanical constriction.

### 2.2. Interface Dynamic Voltage Stability in Response to Constrictions

The interface electrochemical stability is calculated by pseudo-phase approach[12] within the perturbation method framework (see Experimental Section and Figure S2, Supporting Information). The constriction induced dynamic voltage stability model is compatible with high-throughput computational platform to search for promising interface coating materials that can provide enhanced interface dynamic stability. Such coating can provide in situ dynamic decomposition to fix any cracks caused by breathing cathode during cycling.

#### 2.2.1. High-Throughput Search under Constrained Ensemble for Li Sulfide Electrolyte Coating Materials

**Figure 5**a shows the high-throughput screening procedure for searching potential coating materials for interfaces between cathode and sulfide electrolyte materials. We first screened out the materials with radiative elements and removed duplicates to reduce computational cost. The second screening criterion selected stable phase entries with hull energy <5 meV atom$^{-1}$. The third one considers the initial interface chemical stability of coating/pristine cathode and coating/electrolyte. Coatings whose interfacial decomposition energy that are <50 meV atom$^{-1}$ can pass the third screening step. There are 2089 materials that pass the third screening.

Lastly, we examine the electrochemical stability of the interfaces by unconstrained and constrained ensemble pseudo-binary

**Figure 4.** Constriction induced voltage stability of Li solid-state electrolytes calculated by direct minimization method. Voltage window expansion at representative $K_{\text{eff}}$ of sulfides (blue bars), oxides (green bars), and halides (purple bars). The red and blue lines in each bar denote the reduction and oxidation limit of the electrolyte. The numbers on the right of each bar, e.g., 7.3V@20 GPa denote the voltage window at (@) a given $K_{\text{eff}}$. The intensity of each color shows the magnitude of decomposition reaction strain.

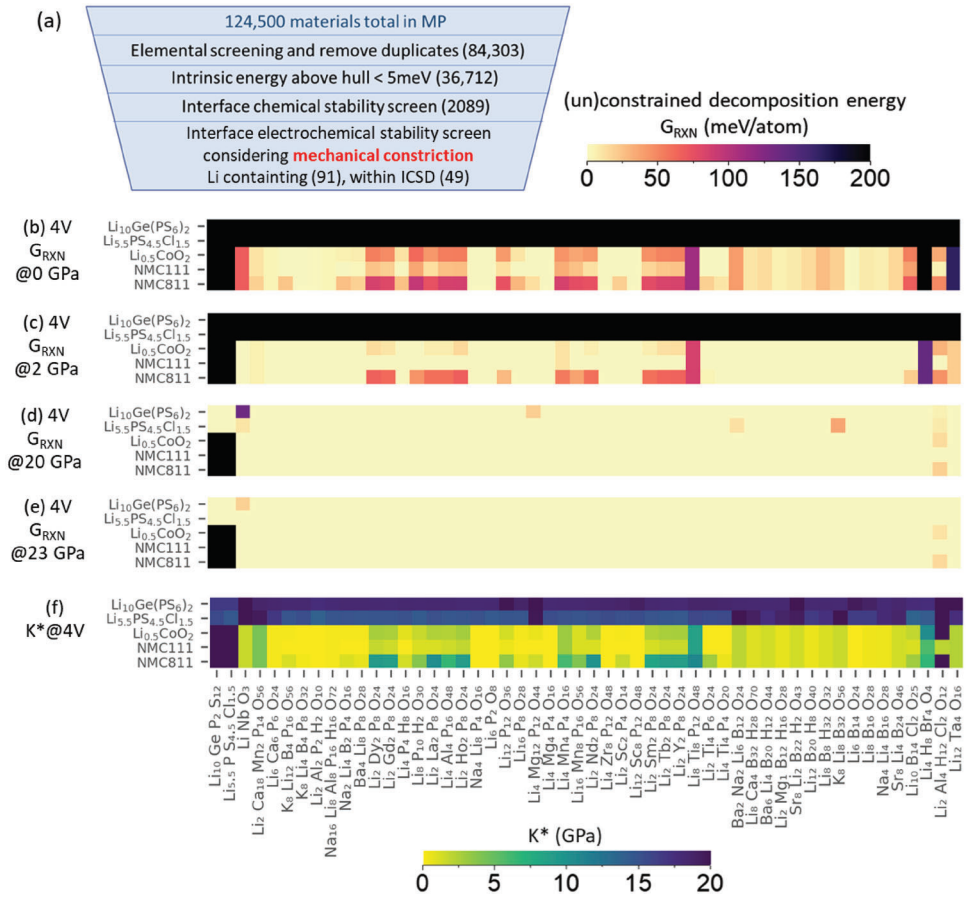


**Figure 5.** High throughput search of coating materials for LGPS, LPSCl electrolytes and 4V-$Li_{0.5}CoO_2$ (LCO), 4V-$Li_{0.5}Ni_{1/3}Mn_{1/3}Co_{1/3}O_2$ (NMC111) and 4V-$Li_{1/3}Ni_{7/9}Mn_{1/9}Co_{1/9}O_2$ (NMC811). a) The high-throughput screening procedure. b–e) Electrochemical decomposition energy of the screened coating at SSE or cathode interfaces, and SSE/cathode interfaces as well, calculated by b) unconstrained ensemble and constrained ensemble at c) $K_{eff}$ = 2 GPa, d) $K_{eff}$ = 20 GPa, e) $K_{eff}$ = 23 GPa. f) The critical effective modulus $K^*$ of each interface.

interface simulations. If the interface electrochemical decomposition energy at 4 V is <50 meV atom$^{-1}$ at $K_{eff}$ = 20 GPa, the material will become a coating candidate to help stabilize cathode interface reaction. We choose 20 GPa because it is a value roughly half of the bulk modulus of sulfide or halide electrolyte materials, which is around the maximum mechanical constriction that can be provided at the solid–solid interface based on the inclusion model.[22] Our goal is thus to predict cathode coating materials that can bring the critical effective modulus $K^*$ below 20 GPa, where a lower $K^*$ below 10 or 5 GPa is in general more preferred, as they make the interface reaction easier to be suppressed by local mechanical constriction $K_{eff}$.

There are 91 Li containing materials that passed all the screening steps. We selected 49 of them that are with ICSD id to present in Figure 5. Figure 5b,e show the interface decomposition energies of 49 candidates plus LGPS, LPSCl and a commonly used coating $LiNbO_3$ for comparison, which is calculated by unconstrained ensemble (0 GPa in Figure 5b), slightly constrained ensemble (2 GPa in Figure 5c), and 20 and 23 GPa constrained ensemble (Figure 5d,e).

Without coating, direct interface between cathode and electrolyte cannot be electrochemically stabilized even at 23 GPa due to small response to constriction as indicated by the large $K^*$ value in Figure 5f. Furthermore, all these coatings are highly electrochemically reactive with LGPS and LPSCl when unconstrained due to the electrochemical intrinsic instability of sulfide electrolytes and the interface reaction between coating and electrolyte. However, these coating interfaces are largely stabilized (< 50 meV atom$^{-1}$) at 20 or 23 GPa of effective constriction modulus.

For the $LiNbO_3$ and cathode interfaces, the decomposition products are just Li, $O_2$, and $Nb_2O_5$, so the interface is in principle stable. However, $LiNbO_3$ itself is thermodynamically unstable at 4 V at 0 GPa. Nevertheless, we find that the 4 V decomposition can be stabilized by a modest 2 GPa constriction. Note that such a small constriction might also be provided by Nb diffusion[46–47] induced surface tension at the cathode particle level in a liquid electrolyte battery, so that although unconstrained at the cell device level, Li-Nb-O coating can still improve the cycling performance of NCM811. Comparing $LiNbO_3$ with other predicted coatings in Figure 5d, $LiNbO_3$ shows the largest K* with LGPS, indicating that these predicted coatings could also be more promising to provide better dynamic voltage stability. For example, Li-Ta-O based coating (right most in the list) can show better rate performance than Li-Nb-O based coating.[48] The predicted Li-B-O based coating has also been proven to improve

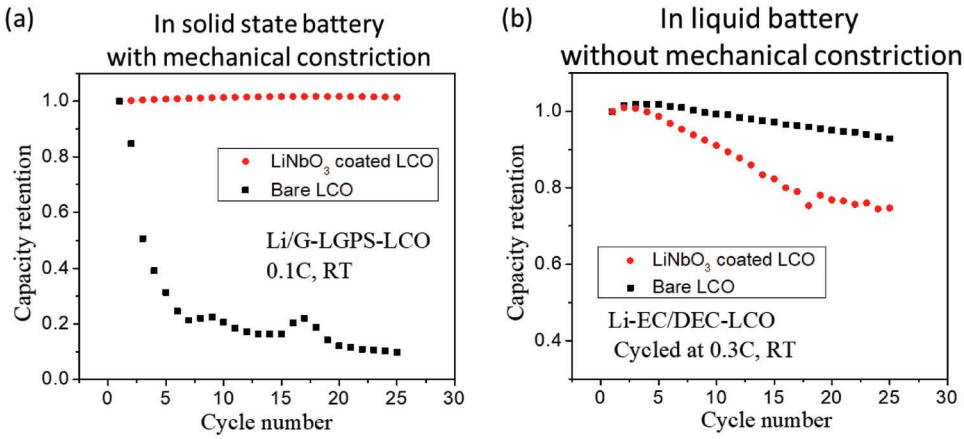


**Figure 6.** Experimental examination of $LiCoO_2$|$LiNbO_3$ interface dynamic stability. a) $LiNbO_3$ coated $LiCoO_2$ (LCO) shows a better cycling performance than bare LCO in solid-state battery with mechanical constriction; b) $LiNbO_3$ coated LCO shows a worse cycling performance than bare LCO in liquid battery without mechanical constriction.

$LiCoO_2$ performance, and can have better first-cycle capacity than Li-Nb-O.[49–50] But since experimentally $LiNbO_3$ coating can be more easily implemented by a simple two-steps method of solution evaporation and calcination,[46] coating a predicted material and achieving better cycling performance than that of $LiNbO_3$-coated one may require some nontrivial innovations in the synthesis and coating procedure.

Here we use $LiNbO_3$|$LiCoO_2$ (LCO) interface as a model system to experimentally demonstrate the importance of dynamic voltage stability in predicting coating materials for solid state batteries. For solid state battery with LGPS as cathode electrolyte (**Figure 6**a), bare LCO shows much worse cycling stability than $LiNbO_3$ coated LCO at room temperature, consistent with our prediction that the LCO and LGPS interface is unstable at any $K_{eff}$ values while $LiNbO_3$ can help stabilize the interface when a nonzero $K_{eff}$ is applied.

Since it is difficult to remove mechanical constriction in a solid-state battery to make $K_{eff} = 0$, we tested liquid electrolyte batteries without mechanical constriction and thus $K_{eff}$ is close to zero (Figure 6b). In contrast, $LiNbO_3$ coated LCO now shows worse cycling stability than bare LCO, consistent with our prediction that $LiNbO_3$ and LCO interface is not stable when $K_{eff}$ is zero. Note that the LCO case discussed here is different from $LiNbO_3$ coated NMC811 mentioned earlier, where the coating does improve the cycling in liquid electrolyte batteries.[46] This may suggest a lack of Nb diffusion induced surface tension in the coated LCO in comparison with coated NMC, as in the NMC case the surface tension can serve as a nonzero $K_{eff}$ in the liquid electrolyte battery to help stabilize the interface between NMC and $LiNbO_3$.

Although coating is a general strategy to improve the interface stability, we found that LCO and $Li(Ni_{0.8}Mn_{0.1}Co_{0.1})O_2$ (NMC811) can sometimes cycle with sulfide electrolytes even without cathode coating.[4,15,16] For such an interface, the initial chemical decomposition interphase should be considered. The interphase is formed by the direct contact between the cathode and electrolyte during powder mixing in mortar and cathode film formation in battery assembly, before the application of voltage for electrochemical reaction.[26] **Figures 7**a,b show such an alternative computational approach by first considering the preformed chemical interphase between the corresponding cathode and electrolyte from pseudo-phase calculation without applying a voltage (See Experimental Section). We then calculate $K^*$ at the interface between the preformed interphase and catholyte at 4 V (Figure 7b), which greatly reduces $K^*$ by orders of magnitude than the direct interface between the solid electrolyte and cathode (Figure 7a). This suggests that these new interphases, once preformed, can make the interface reactions much more easily stabilized at 4 V.

We further tested uncoated LCO and NMC811 cathode with sulfide cathode electrolytes in solid-state batteries. For LCO-LGPS cathode composite, it can barely cycle directly at room temperature with <50 mAh $g^{-1}$ capacity and a fast capacity decay, but surprisingly, we found that it can cycle at 55 °C (Figure 7c). More importantly, after >100 stable cycles at 55 °C, it then can be cycled at room temperature (Figure 7d). We then test the NMC811-sulfide cathode composite with varying temperatures (Figures 7e,f), which shows that NMC811-sulfide can already be cycled directly at room temperature, and high temperature does not improve its subsequent room temperature performance. These results suggest that LCO-sulfide chemical interphase, which serves to stop further decomposition by dynamic voltage stability and improve interface contacts, requires a higher temperature to form than that of NMC811-sulfide.

### *2.2.2. High-Throughput Search under Constrained Ensemble for Li Oxide Electrolyte (LLZO) Coating Materials*

A classic garnet type LLZO is used as an example of oxide electrolyte to explore the interface reaction by constrained ensemble (**Figure 8**). Note that we added an elemental screening to remove the expensive (>50 USD/lb) and toxic elements to narrow down the final list. The challenge for the garnet electrolyte-cathode interface lies in the good contact and low interfacial resistance within low thermal processing window.[51] Binding electrolyte and cathode together with an electrochemically stable coating material is a useful strategy.[52–54] When unconstrained, since LLZO itself is not stable at 4 V, the interfaces with coating materials are mostly unstable with high interfacial reaction energies as

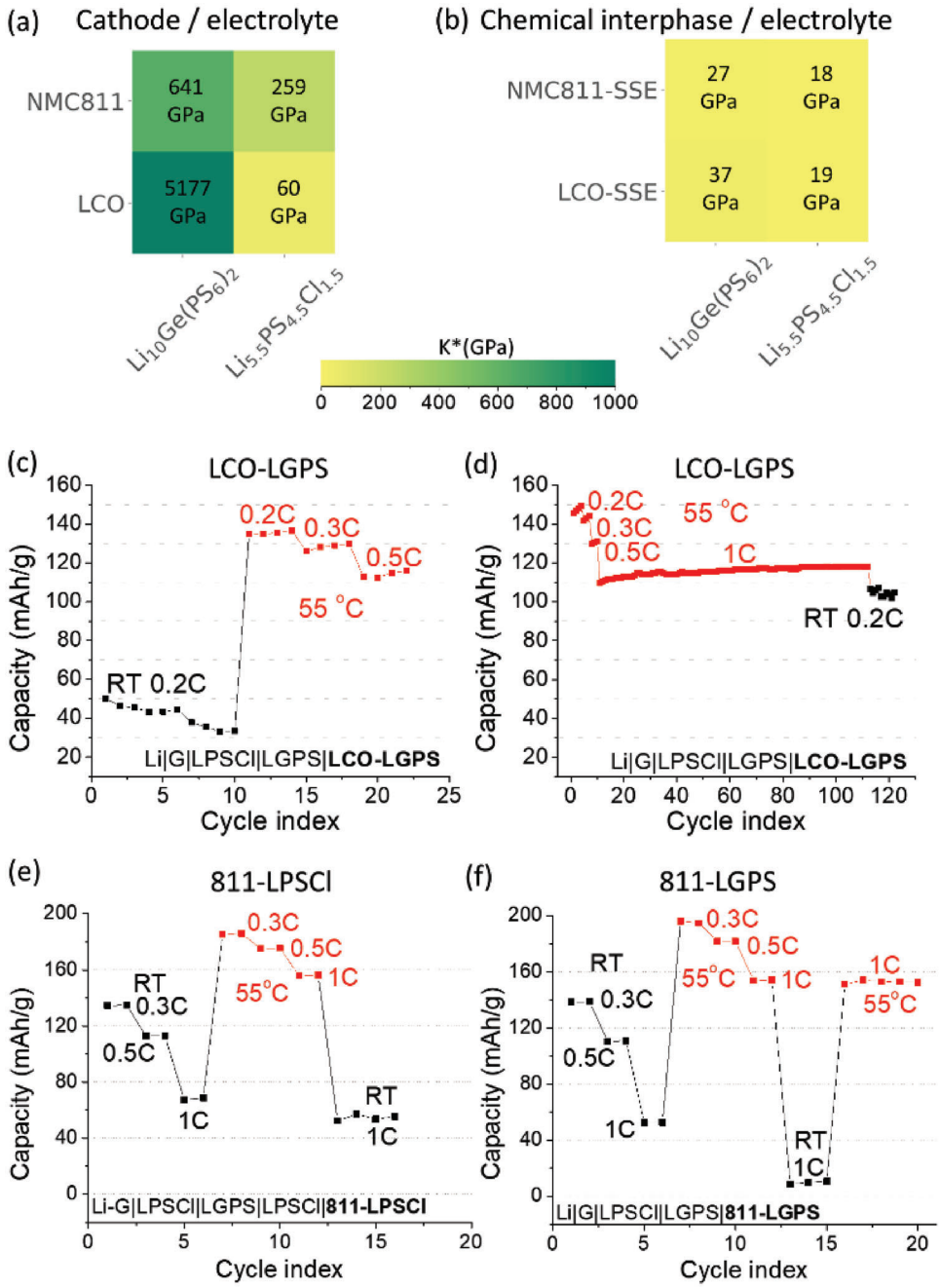


**Figure 7.** a,b) Critical effective modulus ($K^*$) needed to stabilize the cathode / electrolyte electrochemical interface reaction at 4 V with different computational approaches. a) The cathode and electrolyte are in direct contact. b) A chemical interphase is formed first between the cathode and electrolyte, with which the electrolyte is in contact at 4 V. c) LCO-LGPS cathode composite solid-state battery cycling first at room temperature and then at 55 °C and d) the same battery cycled in the reversed temperature sequence. e,f) Temperature varying test for e) 811-LPSCl and 811-LGPS cathode composite cycled in solid-state batteries.

indicated by the black grids. For the four non-black grids, it simply indicates that there is no interfacial reaction between LLZO and the particular coating, with the energy showing the 4 V instability of the coating material itself. For the coating materials that have the same decomposition energies interfacing LCO and NMC (and LLZO if non-black), in most cases the decomposition is from the intrinsic 4 V instability of the coating materials due to a lack of the interfacial mutual reaction. We use $K_{eff}$ = 7 GPa in the screening here since LLZO itself is stabilized at 7 GPa at 4 V. To achieve sufficient $K_{eff}$, a dense contact is required. Softer coatings, such as $Li_2CO_3$ that is also included in the Figure 8 prediction with lower bulk modulus of 63 GPa and shear modulus of 32 GPa (documented in Materials Project), may be a good candidate for minimizing the complexity of oxide processing (such

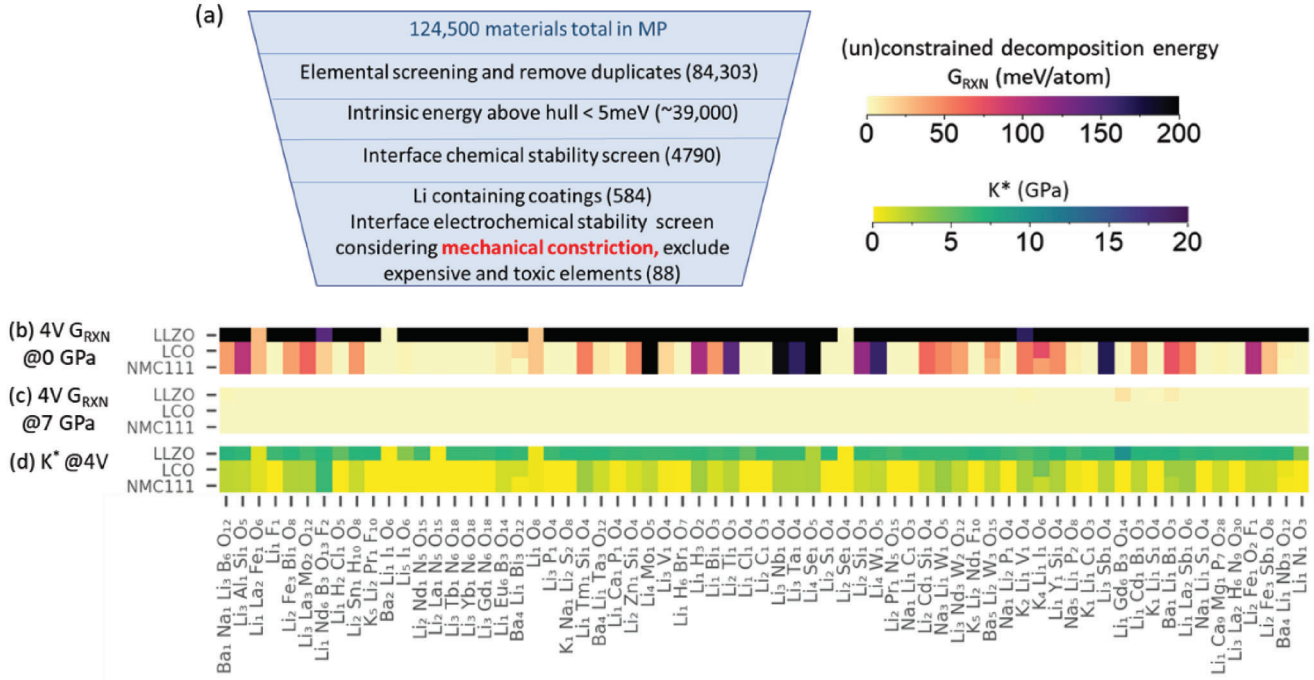


**Figure 8.** High throughput search of coating materials for $Li_7La_3Zr_2O_{12}$ (LLZO) electrolytes and 4V-$Li_{0.5}CoO_2$ (LCO), 4V-$Li_{0.5}Ni_{1/3}Mn_{1/3}Co_{1/3}O_2$ (NMC111) cathodes. a) The high-throughput screening procedure; b,c) Electrochemical decomposition energy of the screened coating/SSE or cathode interfaces, and SSE/cathode interfaces calculated by unconstrained ensemble b) and constrained ensemble at $K_{eff}$ = 7 GPa (c), and d) the critical effective modulus $K^*$ of each interface at 4 V.

as the requirement for high temperature sintering) and for working at high-voltage. Note that $Li_2CO_3$ itself is ionically insulating, which is one reason why the spontaneous formation of $Li_2CO_3$ conformal coating on LLZO in air needs certain engineering,[55] and boron doping that enables Li conduction can make it a good coating material.[53] Another predicted $Li_3PO_4$ coating has also been experimentally examined between NMC811 and LLZTO to show high capacity and stable cycling.[54]

### *2.2.3. High-Throughput Search under Constrained Ensemble for Li Halide Electrolyte Coating Materials*

Similar screening procedure is used here for the interface between cathode and halide electrolyte. Most of the predicted coating materials for halide electrolytes are still oxides. When unconstrained ($K_{eff}$ = 0, **Figure 9**b), $Li_3YBr_6$ and $Li_3InBr_6$ show unstable interfaces in most cases (dark color in Figure 9b), because $Li_3YBr_6$ and $Li_3InBr_6$ are not stable at 4 V, and they also have relatively large $K^*$ as shown in Figure 9d. To stabilize the interface, a $K_{eff}$ = 7 GPa is applied in the last step of the high-throughput screening, since all 6 halide electrolytes themselves are stabilized at 7 GPa. We notice that non-solid $Br_2$ at RT appears in most decomposition products of bromide/coating interfaces, and $ClO_2$ appears in 60% of the chloride/coating decomposition products, which won't really contribute to the solid reaction strain at RT that leads to the prediction above. Similar to the $Li_3YCl_6$ intrinsic stability case (Figure 4), we add $Li_xCl_y$ to possible decomposition products. The list is then shortened from 60 candidates to 46 (Figure S3, Supporting Information), and 42% of the chloride/coating decomposition products includes $Li_xCl_y$ (all $LiCl_3$), while $ClO_2$ appearance drops a little to 50%. Note that $LiCl_3$ and $ClO_2$ can coexist in a decomposition. $ClO_2$ may be reacted to form other new solid compounds such as $Li_xCl_yO_z$ to contribute to the reaction strain. Similarly, other non-solid phases at RT (e.g., $Br_2$) might also end up as $Li_xBr_y$ and $Li_xBr_yO_z$ when nonequilibrium reaction processes are considered that are more likely to happen under ionic passivation from mechanical constriction.

## 3. Conclusion

In this work, we systematically reinvestigated the voltage window response of mechanical constriction of different solid-state electrolytes and more carefully considered nonequilibrium reaction pathways due to ionic passivation. The oxidative limit of sulfide electrolytes can be opened to ≈4 V, where kinetic stability can play an important role together with thermodynamic metastabiltiy for the voltage stabilization. Oxide electrolytes can be opened to >6 V if dense pellet can be achieved, where the additional role of plastic deformation in comparison with sulfides can be better evaluated in experiment. Halide materials have the highest window opening susceptibility upon mechanical constriction, and $Li_xCl_y$ phases may form during decomposition instead of the gas phase $Cl_2$.

By applying constrained ensemble to high-throughput search, we predicted several lists of coatings for Li cathode/electrolyte interfaces for sulfide, oxide, halide electrolytes. For interfaces between sulfide electrolytes and oxide cathodes, coatings with lower critical mechanical modulus $K^*$ than $LiNbO_3$ are predicted.

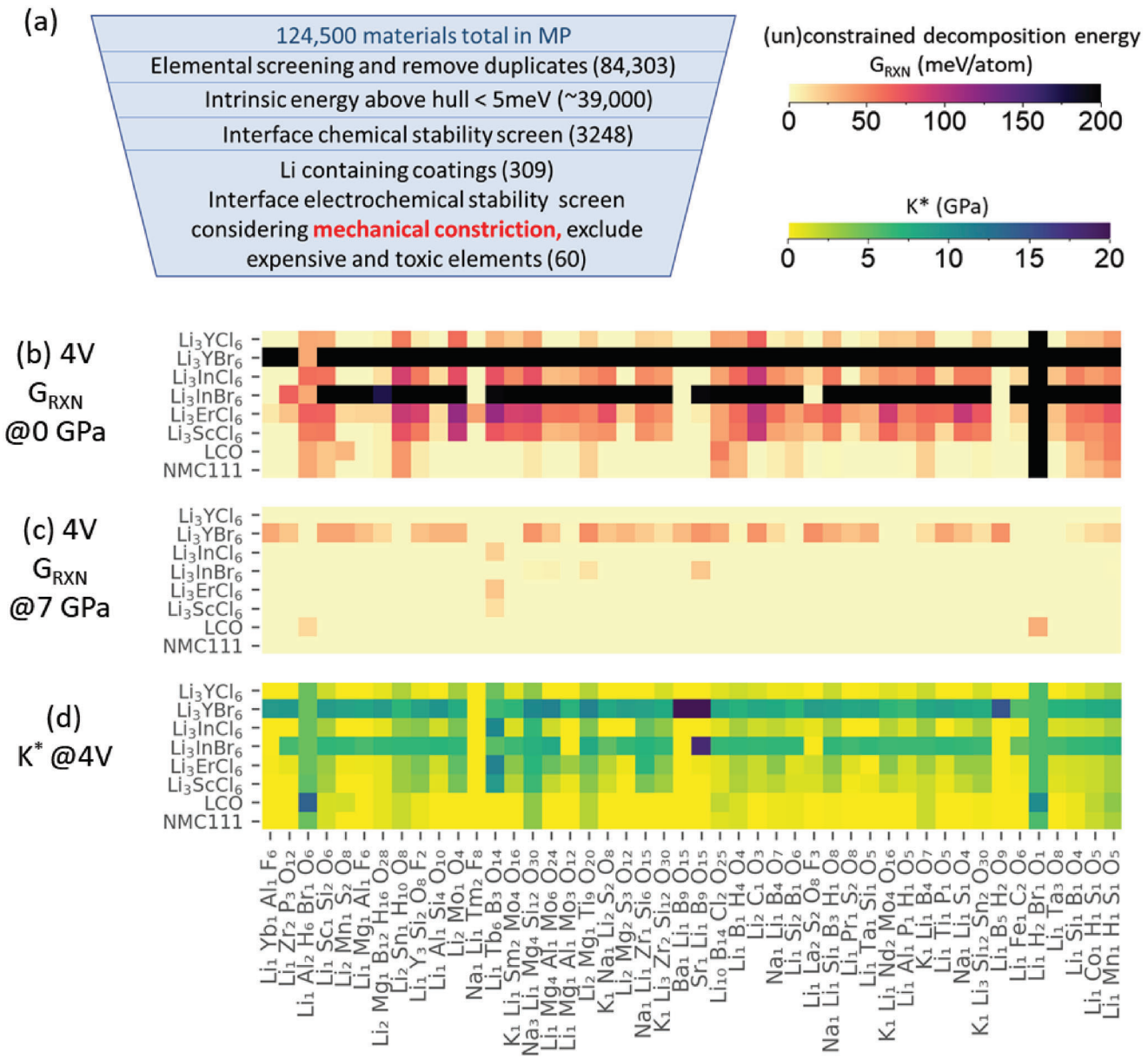


**Figure 9.** High throughput search of coating materials for halide electrolytes and 4V-$Li_{0.5}CoO_2$, 4V-$Li_{0.5}Ni_{1/3}Mn_{1/3}Co_{1/3}O_2$ (NMC111) cathodes. a) The high-throughput screening procedure; Electrochemical decomposition energy of the screened coating/SSE or cathode interfaces, and SSE/cathode interfaces calculated by b) unconstrained ensemble and constrained ensemble at c) $K_{eff}$ = 7 GPa. (d) The critical effective modulus $K^*$ of each interface.

$LiNbO_3$-$LiCoO_2$ interface shows better cyclability in solid state battery than in liquid battery in our experiment, giving experimental evidence of dynamic interface stability related to coating at the solid-solid interface. The fact that some batteries can cycle without coating can be explained by the more stable interfaces with chemically preformed interphase during materials mixing. For oxide materials, potential coating materials that can act as electrochemically stable binder between cathode and garnet electrolyte are in the prediction list, including the reported B-doped $Li_2CO_3$ and $Li_3PO_4$. For halide materials, we discussed the possibility of forming $Li_xCl_y$ at the interface with cathodes. Our work will shed light on the future design of electrolyte and electrode interface reaction by explicitly considering the effect of dynamic voltage stability. An application of the new design strategy in future experiment will further advance the performance of solid-state batteries.

## 4. Experimental Section

*Constrained Ensemble Computational Approach*: The computational modeling for constriction induced voltage stability is illustrated in Figure S4 (Supporting Information) for perturbation (Figure S4a, Supporting Information) and minimization (Figure S4b, Supporting Information) methods, respectively. The study first considered a solid-state electrolyte (SSE) with stability window $U_w$ ($K_{eff}$ = 0) between reduction limit $U_{re}$ ($K_{eff}$ = 0) and oxidation limit $U_{ox}$ ($K_{eff}$ = 0) when being unconstrained

mechanically ($K_{eff} = 0$). Above $U_{ox}$ ($K_{eff} = 0$), oxidation decomposition will happen, where Li ion in solid-state electrolyte decomposes to Li metal. Below $U_{re}$ ($K_{eff} = 0$), reductive decomposition will happen, where external Li metal source from anode was consumed. In perturbation method, at each voltage point only one oxidative (reductive) reaction was considered with the largest decomposition energy.[23] The reaction equation, reaction strain $\epsilon$, and reaction free energy $\Delta G_{EC-RXN}$ can be written as:

$$SSE \rightarrow \sum d_i Dec_i + nLi \tag{1}$$

$$\epsilon = \frac{\sum d_i V_{Dec_i} + nV_{Li} - V_{SSE}}{V_{SSE}} \tag{2}$$

$$\Delta G_{EC-RXN} = G_{Dec} + n(G_{Li} - eU) - G_{SSE} + K_{eff} V_{SSE} \epsilon \tag{3}$$

In Equation (1), $Dec_i$ denotes the i$^{th}$ decomposition product and $d_i$ is its stoichiometry. In Equation (2), the reaction strain is defined as the fraction of the difference between the final volume and the initial volume. Note that the reactant volume of Li metal in the reduction reaction at anode is not counted in the calculation of reaction strain, but Li metal product volume in the oxidative reaction at cathode is counted. Below the reduction limit, Li metal reactant was absorbed into the SSE to form the interface reaction decomposition, which contributed to the local volume expansion of the decomposition and the formation of the plastic strain field surrounding the decomposition reaction front that was of importance to the dynamic voltage stability of interest here. Since Li metal reactant initially was not inside the region of SSE, the volume of lithium metal reactant was thus not counted in the calculation of reaction strain that was inside SSE. Outside the region of the reaction front, $Li^+$ ion and electron could still leave the anode region from the ion and electron reservoir to complete the reduction reaction as also required by the eU term in Equation (3), which, however, did not influence the local positive reaction strain of the interface reaction, as all decomposition products were encapsulated by the ionically passivated reaction front layer. Similarly, beyond oxidation limit, although electron should go through outside circuit from cathode to anode side and then combine with a $Li^+$ that was migrated from the Li reservoir at cathode to the anode, the electron and Li ion left the cathode were not from the reaction product of Li metal but from the reservoir outside the decomposition region encapsulated by the reaction front. $Li^+$ ions as reaction product were trapped in the cathode decomposition region encapsulated by the ionically passivated reaction front layer, which then could combine with a neighboring electron to form Li metal. Li metal product in oxidative reaction thus contributed to the positive reaction strain.

In Equation (3), $G_{Dec} = \sum d_i G_{Dec_i}$, where $G_{Dec_i}$ is the phase energy calculated by DFT obtained from the Materials Project. $U$ is the voltage and the term $K_{eff} V_{SSE} \epsilon$ denotes the mechanical constriction effect where $K_{eff}$ is the effective bulk modulus,[23] $V_{SSE}$ is the volume of solid electrolyte and $\epsilon$ is the reaction strain, so at a given $K_{eff}$, the positive increase of reaction energy is proportional to reaction strain. Figure S4a (Supporting Information) depicts the relationship described by Equation (3). The rimless blue or red dots show the reductive or oxidative decomposition energy at each voltage point at $K_{eff} = 0$, while the rimmed dots show the constrained decomposition energy. The upward arrow represents the magnitude of energy increase calculated from $K_{eff} V_{SSE} \epsilon$.

At $K_{eff} > 0$, if $\Delta G_{EC-RXN}(U)$ is moved from negative to positive values due to the positive $K_{eff} V_{SSE} \epsilon$, then the decomposition will not happen anymore, and the voltage $U$ will be included into the expanded voltage window. Thus, the new voltage range from $U_{re}$ ($K_{eff} > 0$) to $U_{ox}$ ($K_{eff} > 0$) defined by the two new reactions in Figure S4a (Supporting Information) is the voltage window $U_w$ ($K_{eff} > 0$) under certain mechanical constriction. In general, the voltage stability window $U_w$ can be defined as:

$$U_w\left(K_{eff}\right) = U_{ox}\left(K_{eff}\right) - U_{re}\left(K_{eff}\right) \tag{4}$$

The perturbation method only considers reactions with the largest decomposition energy, so that it is computationally effective. However, in reality, there are often more than one decomposition reactions competing in the reaction space with various reaction strains, which means other decomposition reactions with smaller positive reaction strains or even negative reaction strains that are neglected in the perturbation method could happen at voltages between $U_{re}$ (0) and $U_{re}$ ($K_{eff} > 0$), and between $U_{ox}$ (0) and $U_{ox}$ ($K_{eff} > 0$).

A more robust approach named direct minimization method is used to consider all reactions in the reaction space.[23] Figure S4b (Supporting Information) shows an example of implementing minimization method to calculate the voltage window of LGPS. One pair of oxidative and reductive decompositions decide the voltage window at a given $K_{eff}$. Electrochemical reaction energy of two pairs of decompositions corresponding to $K_{eff} = 0$ GPa and $K_{eff} = 10$ GPa are plotted in Figure S4b (Supporting Information) as a straight line in the $\Delta G_{EC-RXN}$-$U$ space defined by Equation (3), whose reaction equations can be expressed in the form of Equation (1) as following:

(a) Reaction 1: $Li_{10}GeP_2S_{12} = 10\ Li + 3\ S + P_2S_7 + GeS_2$
(b) Reaction 2: $Li_{10}GeP_2S_{12} = 1.2\ Li + 0.2\ S + 0.2\ P_2S_7 + 0.2\ Li_4GeS_4 + 0.8\ Li_{10}GeP_2S_{12}$
(c) Reaction 3: $Li_{10}GeP_2S_{12} = 12\ Li_2S + Ge + 2\ P - 14\ Li$
(d) Reaction 4: $Li_{10}GeP_2S_{12} = 6.86\ Li_2S + 0.19\ GeP_3 + 0.81GeS + 1.44\ Li_2PS_3 - 6.6\ Li$

The x-interceptions of the reaction energy straight lines are the stability voltage limits, which can be expressed by equating Equation (4) to 0:

$$U = (G_{Dec} + nG_{Li} - G_{SSE} + K_{eff} V_{SSE} \epsilon) / (ne) \tag{5}$$

The slope is the negative stoichiometry of Li (-$n$) in the Equation (3), and the positive increase of the decomposition energy by mechanical constriction is proportional to reaction strain $\epsilon$, therefore the horizontal shifts are proportional to their $\epsilon/n$. If the reaction strain is negative, void will form and the constriction effect will disappear locally, thus the $K_{eff} V_{SSE} \epsilon$ term will become 0 instead of being negative. This means the voltage window will not change, or equivalently we can define $\epsilon = 0$ in this case.

Reactions (1) and (2) are oxidative decompositions, and reactions (3) and (4) are reductive decompositions. Reactions (1) and (3) decide the voltage window at $K_{eff} = 0$ GPa, and the reactions (2) and (4) decide the voltage window at $K_{eff} = 10$ GPa. Other reactions in the reaction space besides these four are not discussed here since it turns out that they do not determine the voltage window for LGPS here. But we should keep in mind that they do exist in the energy landscape, and solid-state electrolyte can decompose into other products if different voltage and $K_{eff}$ values are applied, or nonequilibrium decomposition pathways override such thermodynamic metastable decompositions.

For this specific case illustrated in Figure S4b (Supporting Information), at $K_{eff} = 0$ GPa, started from any voltage inside the voltage window, when scanning the voltage toward 0 V, the x-interception $U_{re}$ (0) will be met first, where all other reactions (e.g., reaction (4)) in the reaction space except reaction (3) have positive reaction energy so that they are thermodynamically prohibited. Slightly below that voltage $U_{re}$ (0), the energy of reaction (3) becomes negative so LGPS become unstable and will decompose to $Li_2S$, Ge and P. Thus $U_{re}$ (0) is the reductive limit of LGPS at $K_{eff} = 0$ GPa.

When increasing $K_{eff}$ to 10 GPa, the energy of all reactions will increase proportionally to their reaction strain (if positive) as described by Equation (3) and indicated by the four arrows in Figure S4b (Supporting Information). Reaction (3) with reaction strain as large as 25% increases a lot as indicated by the long blue arrow. When scanning voltage toward 0 V at $K_{eff} = 10$ GPa, the x-interception $U_{re}$ (10) belonging to reaction (4) will be met first instead. Reaction (4) has slightly more positive $\Delta G_{EC-RXN}$ than reaction 3 at $K_{eff} = 0$ GPa below $U_{re}$ (0), but after applying mechanical constriction of $K_{eff} = 10$ GPa, its much smaller reaction strain of 6% causes a much smaller positive increase of energy. Note that the slope (-$n$) of the energy line of reaction 4 (-$n_4$ = 6.6) is smaller than that of reaction 3 (-$n_3$ = 14), and the horizontal shift of x-interception is proportional to $\epsilon/n$. The fact that the x-interception of reaction (4) is to the right of the

x-interception of reaction 3 at $K_{eff}$ = 10 GPa is mainly due to the much smaller reaction strain of reaction (4) than reaction (3). The competition between the two oxidization reactions (1) and (2) controlled by $K_{eff}$ follows a similar discussion.

With the illustration discussed above, we can more generally define $U_{re}$ ($K_{eff}$) and $U_{ox}$ ($K_{eff}$). Each decomposition reaction has a *n* value, so we can scan *n* to scan all decompositions:

$$U_{re}\left(K_{eff}\right) = \max_{n<0}[(G_{Dec} + nG_{Li} - G_{SSE} + K_{eff}V_{SSE}\varepsilon)/(ne)] \quad (6)$$

$$U_{ox}\left(K_{eff}\right) = \min_{n>0}[(G_{Dec} + nG_{Li} - G_{SSE} + K_{eff}V_{SSE}\varepsilon)/(ne)] \quad (7)$$

A pseudo-phase[12] composed of *x* coating and (1-*x*) SSE is denoted as *pp*(*x*). DFT phase energy $G_{pp(x)}$, composition *x*, and volume $V_{pp(x)}$ of the *pp*(*x*) are interpolated from coating and SSE. Equation (3) can then be rewritten as:

$$\Delta G_{EC-RXN}(x) = G_{Dec} + n(G_{Li} - eU) - G_{pp(x)} + K_{eff}V_{SSE}\varepsilon \quad (8)$$

Let Equation (8) equal to zero, it gives the critical $K_{eff}$, i.e., $K_{crit}$, that prohibits the electrochemical decomposition of the interface, and the maximum value of $K_{crit}(x)$ to prevent decomposition at all *x* composition is defined as *K**:

$$K_{crit}(x) = -\frac{G_{Dec} + n(G_{Li} - U) - G_{pp(x)}}{V_{pp(x)}\epsilon_x} \quad (9)$$

$$K^* = \max K_{crit}(x) \quad (10)$$

More detailed illustration regarding pseudo-phase approach and critical modulus K* by a computational example can be found in Figure S2 (Supporting Information).

*Battery Assembly and Test*: $Li_{5.5}PS_{4.5}Cl_{1.5}$, was prepared by ball milling and solid-state reactions. Stoichiometric amounts of $Li_2S$ (99.9% purity, Alfa Aesar), $P_2S_5$ (99% purity, Sigma Aldrich), and LiCl (>99% purity, Alfa Aesar) were milled for 16 h under argon protection. The precursor was transferred into a quartz tube and annealed at 550 °C for 1 h with a temperature increasing rate of 5 °C $min^{-1}$ in an argon gas flow. $LiNi_{0.83}Mn_{0.06}Co_{0.11}O_2$ (NMC811) and LGPS (325 mesh) were purchased from MSE. $LiCoO_2$ was purchased from Sigma-Aldrich.

Solid state batteries were made with the configuration of Li/graphite-solid electrolyte layer(s)-cathode matrix. The Li metal foil of 0.63 cm diameter and 25 um thickness (0.42 mg, 1.62 mAh, 5.2 mAh $cm^{-2}$) was covered by a graphite thin film of 0.95 cm diameter to act as the anode. The graphite layer was made by mixing 95 wt% graphite (BTR, China) with 5 wt% PTFE, and the capacity ratio of lithium to graphite is 2.5:1. 30 mg LPSCl (120 µm thickness) and 100 mg central layer powder (400 µm thickness) were applied as the electrolyte. A 60 mg separating layer (240 µm) of the same electrolyte powder in the cathode matrix was added when the central layer was different from that in the cathode matrix. $LiNbO_3$ (LNO) was coated on $LiNi_{0.83}Mn_{0.06}Co_{0.11}O_2$ (NMC811) or $LiCoO_2$ (LCO) by 1.9 wt% following previous report.[46] Bare 811 (70 wt%), bare LCO, or LNO coated 811 or $LiCoO_2$ was mixed with 30 wt% LPSCl or LGPS to serve as the cathode with an additional 3% PTFE to make a cathode film. The loading of the cathode was kept at 2 mg $cm^{-2}$ for all the battery tests. The battery was initially pressed at 460 MPa and a stack pressure of 150 MPa was maintained by a pressurized cell. The batteries were cycled at 55 °C or room temperature on an Arbin battery testing station in an environmental chamber with the humidity controlled <10% inside Memmert hpp110, 1 C-rate = 150 mA $g^{-1}$ in this work. Liquid electrolyte batteries used glass fiber as separator and 1 M LiPF6 in EC/DMC (v:v = 1:1) as electrolyte. Li metal is used as anode. The powder of cathode active material, carbon black, and PTFE were mixed with weight ratio of 85:10:5 and then rolled into a thin film with diameter of 5/16″, and then assembled in a Swagelok cell.

## Supporting Information

Supporting Information is available from the Wiley Online Library or from the author.

## Acknowledgements

This work is partially supported by Data Science Initiative Competitive Research Award at Harvard University, and partially supported by the Assistant Secretary for Energy Efficiency and Renewable Energy (EERE), Vehicle Technology Office (VTO) of the U.S. Department of Energy (DOE), and Nissan North America. This work was supported by computational resources from the National Science Foundation Extreme Science and Engineering Discovery Environment (XSEDE) Stampede and Frontera supercomputers.

## Conflict of Interest

The authors declare no conflict of interest.

## Data Availability Statement

The data that support the findings of this study are available from the corresponding author upon reasonable request.

## Keywords

coating, dynamic voltage stability, interfaces, solid-state batteries

Received: July 17, 2023
Revised: August 13, 2023
Published online:

[1] Y. Chen, Z. Wang, X. Li, X. Yao, C. Wang, Y. Li, W. Xue, D. Yu, S. Y. Kim, F. Yang, A. Kushima, G. Zhang, H. Huang, N. Wu, Y.-W. Mai, J. B. Goodenough, J. Li, *Nature* **2020**, *578*, 251.
[2] Y.-G. Lee, S. Fujiki, C. Jung, N. Suzuki, N. Yashiro, R. Omoda, D.-S. Ko, T. Shiratsuchi, T. Sugimoto, S. Ryu, J. H. Ku, T. Watanabe, Y. Park, Y. Aihara, D. Im, I. T. Han, *Nat. Energy* **2020**, *5*, 299.
[3] L. R. Mangani, C. Villevieille, *J. Mater. Chem. A* **2020**, *8*, 10150.
[4] L. Ye, X. Li, *Nature* **2021**, *593*, 218.
[5] L. Ye, W. Fitzhugh, E. Gil-González, Y. Wang, Y. Su, H. Su, T. Qiao, L. Ma, H. Zhou, E. Hu, X. Li, *Adv. Energy Mater.* **2020**, *10*, 2001569.
[6] T. Asano, A. Sakai, S. Ouchi, M. Sakaida, A. Miyazaki, S. Hasegawa, *Adv. Mater.* **2018**, *30*, 1803075.
[7] X. Li, J. Liang, J. Luo, M. N. Banis, C. Wang, W. Li, S. Deng, C. Yu, F. Zhao, Y. Hu, *Energy Environ. Sci.* **2019**, *12*, 2665.
[8] Y. Xiao, L. J. Miara, Y. Wang, G. Ceder, *Joule* **2019**, *3*, 1252.
[9] Y. Zhu, X. He, Y. Mo, *ACS Appl. Mater. Interfaces* **2015**, *7*, 23685.
[10] S. P. Ong, Y. Mo, W. D. Richards, L. Miara, H. S. Lee, G. Ceder, *Energy Environ. Sci.* **2013**, *6*, 148.
[11] S. Wang, Q. Bai, A. M. Nolan, Y. Liu, S. Gong, Q. Sun, Y. Mo, *Angew. Chem., Int. Ed.* **2019**, *58*, 8039.
[12] W. D. Richards, L. J. Miara, Y. Wang, J. C. Kim, G. Ceder, *Chem. Mater.* **2016**, *28*, 266.
[13] F. Du, X. Ren, J. Yang, J. Liu, W. Zhang, *J. Phys. Chem. C* **2014**, *118*, 10590.
[14] T. K. Schwietert, V. A. Arszelewska, C. Wang, C. Yu, A. Vasileiadis, N. J. de Klerk, J. Hageman, T. Hupfer, I. Kerkamm, Y. Xu, *Nat. Mater.* **2020**, *19*, 428.

[15] Y. Wang, L. Ye, X. Chen, X. Li, *JACS Au* **2022**, *2*, 886.
[16] E. Gil-González, L. Ye, Y. Wang, Z. Shadike, Z. Xu, E. Hu, X. Li, *Energy Storage Mater.* **2022**, *45*, 484.
[17] J. Sung, S. Y. Kim, A. Harutyunyan, M. Amirmaleki, Y. Lee, Y. Son, J. Li, *Adv. Mater.* **2023**, *35*, 2210835.
[18] J. Woo, Y. B. Song, H. Kwak, S. Jun, B. Y. Jang, J. Park, K. T. Kim, C. Park, C. Lee, K. H. Park, *Adv. Energy Mater.* **2023**, *13*, 2203292.
[19] D. H. S. Tan, Y.-T. Chen, H. Yang, W. Bao, B. Sreenarayanan, J.-M. Doux, W. Li, B. Lu, S.-Y. Ham, B. Sayahpour, J. Scharf, E. A. Wu, G. Deysher, H. E. Han, H. J. Hah, H. Jeong, J. B. Lee, Z. Chen, Y. S. Meng, *Science* **2021**, *373*, 1494.
[20] D. Cao, X. Sun, Y. Li, A. Anderson, W. Lu, H. Zhu, *Adv. Mater.* **2022**, *34*, 2200401.
[21] F. Wu, W. Fitzhugh, L. Ye, J. Ning, X. Li, *Nat. Commun.* **2018**, *9*, 4037.
[22] W. Fitzhugh, F. Wu, L. Ye, H. Su, X. Li, *Small* **2019**, *15*, 1901470.
[23] W. Fitzhugh, L. Ye, X. Li, *J. Mater. Chem. A* **2019**, *7*, 23604.
[24] Y. Su, L. Ye, W. Fitzhugh, Y. Wang, E. Gil-González, I. Kim, X. Li, *Energy Environ. Sci.* **2020**, *13*, 908.
[25] F. P. McGrogan, T. Swamy, S. R. Bishop, E. Eggleton, L. Porz, X. Chen, Y. M. Chiang, K. J. Van Vliet, *Adv. Energy Mater.* **2017**, *7*, 1602011.
[26] W. Fitzhugh, X. Chen, Y. Wang, L. Ye, X. Li, *Energy Environ. Sci.* **2021**, *14*, 4574.
[27] N. Kamaya, K. Homma, Y. Yamakawa, M. Hirayama, R. Kanno, M. Yonemura, T. Kamiyama, Y. Kato, S. Hama, K. Kawamoto, *Nat. Mater.* **2011**, *10*, 682.
[28] P. Bron, S. Johansson, K. Zick, J. r. Schmedt auf der Günne, S. Dehnen, B. Roling, *J. Am. Chem. Soc.* **2013**, *135*, 15694.
[29] Y. Seino, T. Ota, K. Takada, A. Hayashi, M. Tatsumisago, *Energy Environ. Sci.* **2014**, *7*, 627.
[30] B. Zhang, L. Yang, L.-W. Wang, F. Pan, *Nano Energy* **2019**, *62*, 844.
[31] Y. Kato, S. Hori, T. Saito, K. Suzuki, M. Hirayama, A. Mitsui, M. Yonemura, H. Iba, R. Kanno, *Nat. Energy* **2016**, *1*, 16030.
[32] Z. Liu, W. Fu, E. A. Payzant, X. Yu, Z. Wu, N. J. Dudney, J. Kiggans, K. Hong, A. J. Rondinone, C. Liang, *J. Am. Chem. Soc.* **2013**, *135*, 975.
[33] P. Adeli, J. D. Bazak, K. H. Park, I. Kochetkov, A. Huq, G. R. Goward, L. F. Nazar, *Angew. Chem., Int. Ed.* **2019**, *58*, 8681.
[34] R. Schlem, S. Muy, N. Prinz, A. Banik, Y. Shao-Horn, M. Zobel, W. G. Zeier, *Adv. Energy Mater.* **2020**, *10*, 1903719.
[35] J. Liang, X. Li, S. Wang, K. R. Adair, W. Li, Y. Zhao, C. Wang, Y. Hu, L. Zhang, S. Zhao, *J. Am. Chem. Soc.* **2020**, *142*, 7012.
[36] H. Aono, N. Imanaka, G.-y. Adachi, *Acc. Chem. Res.* **1994**, *27*, 265.
[37] H. Geng, A. Mei, Y. Lin, C. Nan, *Mater. Sci. Eng., B* **2009**, *164*, 91.
[38] R. Murugan, V. Thangadurai, W. Weppner, *Angew. Chem., Int. Ed.* **2007**, *46*, 7778.
[39] Y. Zhao, L. L. Daemen, *J. Am. Chem. Soc.* **2012**, *134*, 15042.
[40] Z. Xu, X. Chen, H. Zhu, X. Li, *Adv. Mater.* **2022**, *34*, 2207411.
[41] S. Muy, J. C. Bachman, L. Giordano, H.-H. Chang, D. L. Abernathy, D. Bansal, O. Delaire, S. Hori, R. Kanno, F. Maglia, *Energy Environ. Sci.* **2018**, *11*, 850.
[42] Y. Gao, S. Sun, X. Zhang, Y. Liu, J. Hu, Z. Huang, M. Gao, H. Pan, *Adv. Funct. Mater.* **2021**, *31*, 2009692.
[43] M. Braga, J. A. Ferreira, V. Stockhausen, J. Oliveira, A. El-Azab, *J. Mater. Chem. A* **2014**, *2*, 5470.
[44] X. Lü, J. W. Howard, A. Chen, J. Zhu, S. Li, G. Wu, P. Dowden, H. Xu, Y. Zhao, Q. Jia, *Adv. Sci.* **2016**, *3*, 1500359.
[45] W. Zhang, A. R. Oganov, A. F. Goncharov, Q. Zhu, S. E. Boulfelfel, A. O. Lyakhov, E. Stavrou, M. Somayazulu, V. B. Prakapenka, Z. Konôpková, *Science* **2013**, *342*, 1502.
[46] F. Xin, H. Zhou, X. Chen, M. Zuba, N. Chernova, G. Zhou, M. S. Whittingham, *ACS Appl. Mater. Interfaces* **2019**, *11*, 34889.
[47] F. Xin, H. Zhou, Y. Zong, M. Zuba, Y. Chen, N. A. Chernova, J. Bai, B. Pei, A. Goel, J. Rana, *ACS Energy Lett.* **2021**, *6*, 1377.
[48] J. S. Lee, Y. J. Park, *ACS Appl. Mater. Interfaces* **2021**, *13*, 38333.
[49] S. H. Jung, K. Oh, Y. J. Nam, D. Y. Oh, P. Brüner, K. Kang, Y. S. Jung, *Chem. Mater.* **2018**, *30*, 8190.
[50] E. A. Wu, C. Jo, D. H. Tan, M. Zhang, J.-M. Doux, Y.-T. Chen, G. Deysher, Y. S. Meng, *J. Electrochem. Soc.* **2020**, *167*, 130516.
[51] K. J. Kim, J. L. Rupp, *Energy Environ. Sci.* **2020**, *13*, 4930.
[52] K. Park, B.-C. Yu, J.-W. Jung, Y. Li, W. Zhou, H. Gao, S. Son, J. B. Goodenough, *Chem. Mater.* **2016**, *28*, 8051.
[53] F. Han, J. Yue, C. Chen, N. Zhao, X. Fan, Z. Ma, T. Gao, F. Wang, X. Guo, C. Wang, *Joule* **2018**, *2*, 497.
[54] Z. Zhao, Z. Wen, X. Liu, H. Yang, S. Chen, C. Li, H. Lv, F. Wu, B. Wu, D. Mu, *Chem. Eng. J.* **2021**, *405*, 127031.
[55] H. Huo, J. Luo, V. Thangadurai, X. Guo, C.-W. Nan, X. Sun, *ACS Energy Lett.* **2019**, *5*, 252.